



Tunable-frequency three-dimensional structured illumination microscopy with reduced data-acquisition

ANA DOBLAS,^{1,3} HASTI SHABANI,^{1,3} GENARO SAAVEDRA,² AND CHRYSANTHE PREZA^{1,*}

¹Computational Imaging Research Laboratory, Department of Electrical and Computer Engineering, University of Memphis, Memphis, TN 38152, USA

²3D Imaging and Display Laboratory, Department of Optics, University of Valencia, Burjassot, E-46100, Spain

³These authors contributed equally to this work

*cpreza@memphis.edu

Abstract: The performance of a tunable three-dimensional (3D) structured illumination microscope (SIM) system and its ability to provide simultaneously super-resolution (SR) and optical-sectioning (OS) capabilities are investigated. Numerical results show that the performance of our 3D-SIM system is comparable with the one provided by a three-wave interference SIM, while requiring 40% fewer images for the reconstruction and providing frequency tunability in a cost-effective implementation. The performance of the system has been validated experimentally with images from test samples, which were also imaged with a commercial SIM based on incoherent-grid projection for comparison. Restored images from data acquired from an axially-thin fluorescent layer show a 1.6× improvement in OS capability compared to the commercial instrument while results from a fluorescent tilted USAF target show the OS and SR capabilities achieved by our system.

© 2018 Optical Society of America under the terms of the [OSA Open Access Publishing Agreement](#)

1. Introduction

Three-dimensional (3D) structured illumination microscopy (SIM) is a well-known method used to improve axial and lateral resolution beyond the diffraction limit in conventional widefield fluorescence microscopy [1]. Gustafsson *et al.* [1] demonstrated that illuminating a fluorescent sample with a structured illumination (SI) pattern, generated from the interference of three mutually-coherent beams emerging from a diffraction grating, enables detection of frequencies beyond the compact support of the optical transfer function (OTF) of the conventional system. This information can be properly demodulated from a set of five SIM images acquired from the same field of view (FoV) of a sample by phase shifting the SI pattern and then computing a final restored optical-sectioned image with double lateral and axial resolution. To achieve quasi-isotropic resolution, images in three different orientations of the SI pattern must be acquired resulting in 15 raw SIM images for each FoV of a 3D sample. This technique has been successfully commercialized by several companies and has been used in a variety of biological studies [2–9]. Since the seminal paper in 2008, different research groups have implemented 3D SIM using a spatial light modulator (SLM) in order to tune the lateral modulation frequency of the SI pattern [10–12].

Because super-resolution (SR) SIM represents a promising high-throughput imaging method for revealing nanoscale morphological features in biological studies, we have been working towards a new, simple, compact and cost-effective SI design that provides tunability of the lateral modulation frequency of the structured pattern using a Fresnel biprism. Recently, we have showed proof-of-concept results of this design in an incoherent two-dimensional (2D) SIM system (based on a SI pattern that is constant axially) capable of achieving simultaneously SR and optical sectioning (OS) due to its modulation frequency

tunability using a two-shot data acquisition approach [13]. In this work we present a 3D-SIM system (based on a SI pattern that varies axially) with a clear advantage over the standard 3D-SIM system (in which the SI pattern is obtained as the interference between three waves) [1] in that it only requires acquisition of three raw images per SI orientation instead of five, while providing a comparable performance. As it is known, to achieve 3D isotropic resolution, images in 3 different orientations of the SI pattern must be acquired. This means acquiring 9 raw images per axial plane for our system and 15 for the standard 3D-SIM system [1]. Reducing the number of raw images in SIM to increase data-acquisition speed and reduce photo bleaching effects has been investigated by taking advantage of the redundancy of information in the raw SIM images when dealing with 2D samples [14–19]. All these efforts have focused on computational approaches for 2D data processing using only 4 raw images acquired from each axial plane as follows: (1) one SIM image for each of the three orientations and a single widefield image; or (2) two phase-shifted SIM images from one orientation and one from each of the other two orientations. We expect that this reduction from 9 to 4 images per axial plane is applicable to our 3D-SIM system since the SI pattern in our system has only a single lateral modulation frequency as is the case in 2D-SIM systems. However, in the case of the standard 3D-SIM system [1] 4 raw images are not sufficient as extra axial information is provided by the 3D SI pattern at half of the lateral modulation frequency. Notwithstanding, the reduction in data acquisition offered by our proposed 3D-SIM system is without any doubt a desired feature for the utility of SIM in live-cell imaging [4,11,12]. Furthermore, the proposed design for the 3D SI pattern presented here offers the possibility of designing *at will* a 3D-SIM system matched to the specific needs of a biological application, and thus providing the best system performance. Investigation of this property will be reported in a future publication. Here we validate experimentally the features of the 3D SI pattern and the implementation of a 3D-SIM system using this novel 3D pattern.

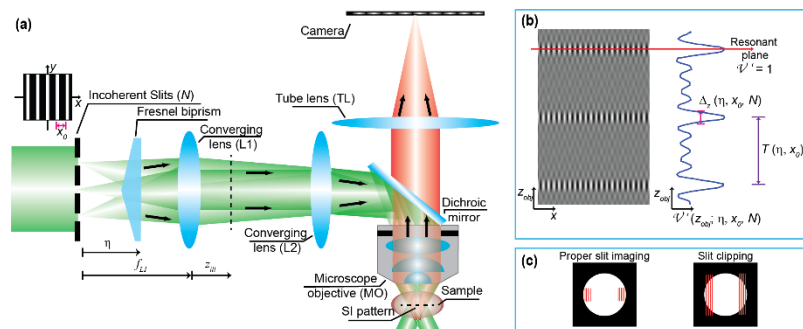


Fig. 1. Tunable-frequency 3D-SIM system based on a Fresnel biprism illuminated by a set of equidistant incoherent slits (N). (a) Illustration of the system. (b) 3D SI pattern with periodic visibility variation [Eq. (2)] created by the system in the sample space (z_{obj}) . High-contrast fringes are located at a set of discrete axial planes. The 3D pattern exhibits a periodic axial contrast and its characteristics are controlled by three system parameters: N , x_0 and η . (c) Illustration demonstrating that improper imaging of the slits in the back focal-plane of the objective lens can lead to clipping of the slits and consequently, to a reduction in the contrast of the fringes. z_{obj} refers to axial coordinate located after L1 lens

2. Fundamentals of tunable-frequency 3D SIM based on Fresnel biprism

2.1 Implementation of tunable-frequency 3D-SIM system

The incoherent tunable-frequency 3D-SIM system presented here uses a SI design based on the illumination of a Fresnel biprism using a properly coded spatially-incoherent source. The source is composed by an array of N mutually-incoherent parallel equidistant slits with the same irradiance [20]. The optical configuration of our current experimental setup is shown in Fig. 1. In this 3D-SIM system, both the lateral and axial modulation frequencies of the 3D

structured pattern can be tuned by axially displacing the biprism. The irradiance distribution of the 3D structured pattern beyond the L1 lens in Fig. 1(b) can be approximated by:

$$e(\mathbf{x}_{ill}, z_{ill}; \eta, x_0, N) \approx 1 + \mathcal{V}'(z_{ill}; \eta, x_0, N) \cos \left[2\pi \frac{a(\eta)}{\lambda f_{L1}} x_{ill} \right], \quad (1)$$

where $\mathbf{x}_{ill} = (x_{ill}, y_{ill})$ and z_{ill} are the transverse and axial coordinates after the L1 lens (e.g. illumination space), x_0 is the lateral distance between two neighboring slits, λ is the source's wavelength, f_{L1} is the focal length of L1 lens and $a(\eta) = 2\eta(n-1)\tan\delta$ is the separation between the two sources created by the Fresnel biprism and depends on the biprism-slits distance (η), the refractive index (n) and the refraction angle (δ) of the biprism. It is important to mention that although Eq. (1) does not provide the full description of the structured pattern since the finite lateral extent of the biprism and the diffraction effect due to the biprism's edge have been neglected [20,21], the axial position of the maxima and minima of $\mathcal{V}'(z_{ill}; \eta, x_0, N)$ is predicted accurately. Also, we have verified that the effect of the envelope function introduced by the biprism's edge is less significant when the Fresnel biprism is illuminated by several spatially-incoherent slits (N).

From Eq. (1) it is clear that the SI pattern varies axially due to $\mathcal{V}'(z_{ill}; \eta, x_0, N)$. Following the same reasoning as in [20], the visibility function, which describes the variation in the fringes' contrast along the axial coordinate, is determined to be as follows:

$$\mathcal{V}'(z_{ill}; \eta, x_0, N) = \frac{\sin(2\pi N w'_m(\eta, x_0) z_{ill})}{N \sin(2\pi w'_m(\eta, x_0) z_{ill})}, \quad (2)$$

where $w'_m(\eta, x_0) = [a(\eta)x_0]/[2\lambda f_{L1}^2]$ is the axial modulation frequency of the pattern. In Eq. (2) we have assumed that the slits' width, Δ , is infinitesimal and, consequently, the maximum of the visibility is always equal to 1. Equation (2) shows that the visibility of the irradiance distribution is a periodic function that only takes maximum values in a discrete set of axial planes [Fig. 1(b)]. Because the slits are set at the front focal-plane of L1 lens, the groups of planes of maximum contrast [$\mathcal{V}'(z_{ill}; \eta, x_0, N) = 1$] referred to here as the resonant planes, are equidistant. The separation between the resonant planes, $T'(\eta, x_0) = 1/w'_m(\eta, x_0)$, changes inversely with both the slits' separation (x_0) and the biprism position (η). Note that the position of the resonant planes and their separation are totally independent of the number of slits (N). In fact, the number of slits affects only the axial extent of the fringes, $\Delta_z(\eta, x_0, N) = 2T'(\eta, x_0)/N$, defined by the region around each resonant plane in which the visibility function is zero. The higher the number of slits, the narrower the axial extent of the fringes.

To verify the performance of our SI device, the optical configuration of Fig. 1(a) has been implemented in an open setup. In our implementation, a custom-made set of slits is illuminated incoherently by the light emerging from a 488-nm laser (Oxxius, RPMC Lasers, Inc., O'Fallon, MO) after passing through a rotating diffuser that removes spatial coherence [22]. The customized slit array fabricated by Ealing Inc. (Scotts Valley, CA) contains 30 slits of 3-mm length and 10- μm width (Δ). The separation between two neighboring slits was specifically fabricated to be $x_0 = 100 \mu\text{m}$. A Fresnel biprism with a 2.5-deg angle (NewLight Photonics, Inc., Toronto, Canada) was inserted between the slit array and a converging lens (L1) of focal length 100 mm. Using a converging lens (L2) of focal length 250 mm and an infinity-corrected objective lens (20 \times Plan NeoFluar of numerical aperture (NA) equal to 0.5, Zeiss), a demagnified replica of the 3D SI pattern obtained after the L1 lens [Eq. (1)] is found in the object space. Note that the system composed by the L2 lens and the objective lens follows a telecentric-afocal configuration. The light emitted by the sample is recollimated again

by the same objective lens and imaged onto a high-sensitivity CMOS camera with $6.5\text{-}\mu\text{m}$ square pixels (Orca-Flash4.0 C11440-22CU, Hamamatsu) using a converging lens (TL lens) of focal length 300 mm. The cutoff frequency ($u_c = 2\text{NA}/\lambda$) of our imaging system is $1.9\ \mu\text{m}^{-1}$ for an emission wavelength of 515 nm and a 0.5 NA lens. With an experimental detection-system lateral magnification, $M = -f_{TL}/f_{MO} = -36.6$, a lateral sampling of $0.178 \times 0.178\ \mu\text{m}^2$ is achieved in the object plane.

In all the experimental studies described here, the sample was mounted onto a motorized linear translation stage (FOC300, PIEZOCONCEPT, Inc. Lyon, France) and its volume was scanned in intervals of $0.3\text{-}\mu\text{m}$. On the other hand, the three needed phase-shifted SIM images were captured by laterally displacing the Fresnel biprism [13] in steps of $4\text{-}\mu\text{m}$, for a single orientation of the SI pattern. As in [13], the lateral modulation frequency of the pattern can be tuned by axially displacing the biprism (η). For this reason, the biprism is mounted onto a separate rail that is parallel to the optical axis.

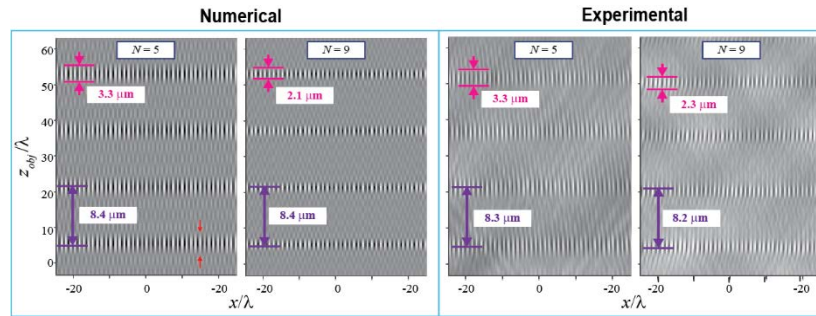


Fig. 2. Experimental and numerical xz -section images of the 3D SI pattern generated using a different number of slits N . The lateral modulation frequency (u_m) for both numerical and experimental results is $\sim 0.8 u_c$ for $u_c = 1.9\ \mu\text{m}^{-1}$. The axial modulation frequency of the 3D SI pattern is $w_m = 0.0156 u_m$.

2.2 Experimental validation of 3D structured illumination (SI) design

By replacing the dichroic mirror in Fig. 1(a) with a beam splitter and using a flat mirror as the object, we acquired images of the 3D SI fringes by axially scanning the sample volume. Figure 2 shows xz -views from the experimental and numerical [computed using Eq. (1) and an illumination lateral magnification of $M_{ill} = -f_{MO}/f_{L2}$] interference patterns created using a different number of slits, i.e. $N = 5$, and 9. As previously predicted, Fig. 2 shows us that the increase of the number of slits (N) produces a decrease of the axial extent of the fringes. Particularly, the experimental axial extent of the fringes, measured by the full-width half-maximum (FWHM) of the axial profile through a resonant plane at a lateral maximum (defined by the red arrows in Fig. 2) has been reduced from $3.3\ \mu\text{m}$ to $2.3\ \mu\text{m}$ as quantified in Fig. 2. Nonetheless, it is important to highlight that the axially-localized fringes are both axially and laterally periodic and these periodicities remain invariant to N . The experimental lateral modulation frequency has been measured as $u_m = (1.50 \pm 0.13)\ \mu\text{m}^{-1} = (0.77 \pm 0.07) u_c$, based on the mean and standard deviation of the four resonant planes shown in Fig. 2. The agreement of this value with the theoretical one, $u_m = a(\eta)/[\lambda f_{L1} M_{ill}] = 1.52\ \mu\text{m}^{-1} = 0.8 u_c$ for $\eta = 56\ \text{mm}$, is high. Regarding the axial periodicity, the distance between two neighboring resonant planes in the experimental results, was determined to be equal to $(8.25 \pm 0.05)\ \mu\text{m}$, which is consistent with the theoretical value, $T(\eta, x_0) = M_{ill}^2 T'(\eta, x_0) = 8.4\ \mu\text{m}$. Note that the difference in these values is less than 2%.

To conclude this comparison, we would like to mention that the contrast of the experimental fringes is not penalized by the increase of the number of slits, see Table 1 in

[23]. This is because the slits have been illuminated in such a way that each point in a slit has its two virtual ones at the aperture stop [i.e., no clipping of the slits occurs as shown in Fig. 1(c)] and, therefore, the fringes' contrast is kept at the maximum value. However, if clipping of some of the virtual slits occurs [Fig. 1(c)], then, for each slit, some point of the coherent pair does not pass through the aperture stop and, therefore, the one which passes will contribute to the background provoking a reduction of the fringes' contrast.

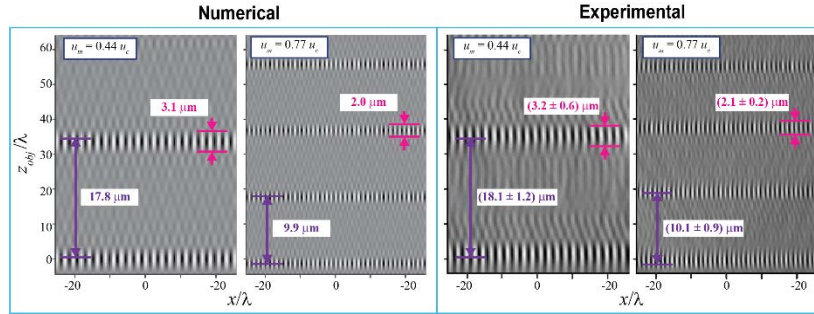


Fig. 3. Numerical and experimental xz -section images of the 3D SI pattern generated using a different lateral modulation frequency (u_m). The axial modulation frequency of the 3D SI pattern is $w_m = 0.0156 u_m$. The cutoff frequency of the system is $u_c = 1.9 \mu\text{m}^{-1}$. The number of slits used was $N = 9$. For the experimental data we report the mean and the standard deviation of the measured axial extent of the fringes computed from 12 axial profiles through the maxima of four different resonant planes.

In this 3D-SIM system, the axial displacement of the biprism (η) controls the lateral modulation frequency (u_m) [13] and the distance between regions of resonant planes (T), which is the inverse of the axial modulation frequency (w_m), and their axial extent (Δ_z). Figure 3 shows the xz -sections of the 3D SI pattern recorded for two different axial positions of the biprism ($\eta = 31 \text{ mm}$ for $u_m = 0.44u_c$; and $\eta = 54 \text{ mm}$ for $u_m = 0.77u_c$) and the same number of slits ($N = 9$). Although the experimental values present a small variation, again, the degree of correlation between simulated and experimental data is very high. These images show a 34% reduction in the axial extent of the fringes when the lateral modulation frequency increases. Thereby, the higher the lateral modulation frequency, the greater the axial confinement of the fringes and the larger the axial modulation frequency. As we will show later, this leads to better out-of-focus light discrimination achieved by the system (i.e, improved OS capability). Again, it is important to mention that the change in the lateral modulation frequency does not affect the fringes' contrast, which means that their visibility is not penalized by the shape of the illumination OTF as in incoherent grid-projection SIM systems [24]. For this experimental data, the measured contrast is 0.53 ± 0.03 for $u_m = 0.44u_c$ and 0.56 ± 0.03 for $u_m = 0.77u_c$.

To conclude the discussion, we would like to highlight the main features of our 3D SI device: (i) the contrast of the fringes is always maximum independent of the slit design (x_0 and N) or the lateral modulation frequency of the pattern (u_m) when clipping is avoided in the pupil plane; (ii) although both the axial modulation frequency and the lateral one are tuned by the position of the biprism, they are still decoupled because the axial modulation frequency can be set at will by changing the slit design (x_0); and (iii) the larger the number of slits (N), the greater the axial confinement of the high-visibility patterns. In addition, to these advantages, the fringes generated by the proposed 3D SI device are unaffected by coherence noise and their lateral modulation frequency can always be tuned to the effective cutoff frequency of the objective lens used. In what follows only experimental results for $N = 9$ slits are shown, which is the maximum number of slits that can be set experimentally at the aperture stop of the $20\times /0.5 \text{ NA}$ objective for the highest lateral modulation frequency ($u_m = 0.8u_c$) and $x_0 = 100 \mu\text{m}$. Note that, for an ideal SIM system (e.g., no penalization through the illumination system and noiseless data acquisition), the fringes' contrast at a lateral

modulation frequency of $u_m = 0.8u_c$ is attenuated by 0.1 (the value of the conventional detection modulation transfer function (MTF) at this frequency [25]) and, therefore, we have considered this frequency as the realistic effective cutoff frequency of an experimental setup.

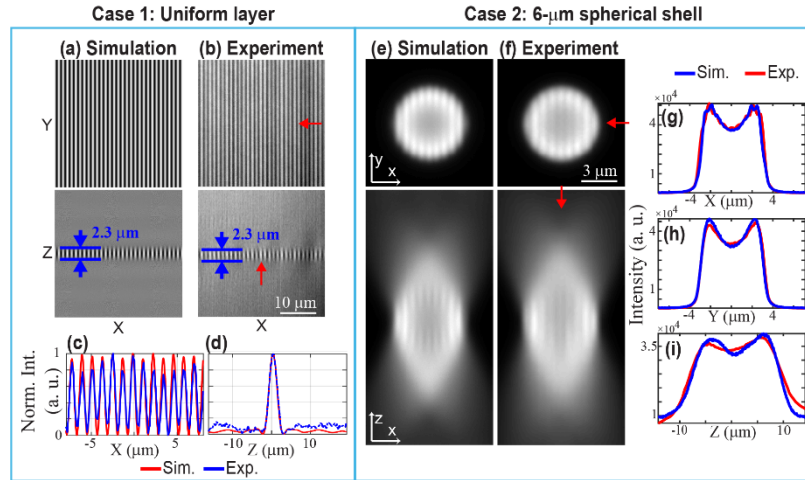


Fig. 4. Evaluation of the experimental 3D-SIM system ($N = 9$ slits) through comparison of experimental and numerical [Eq. (3)] 3D forward images of a fluorescent uniform layer (Case 1) and a 6- μm spherical shell (Case 2). Case 1: xy and xz views of the numerical (a) and experimental (b) 3D image; normalized lateral (c) and axial (d) intensity profile through the center (marked by the red arrows) of the xy and xz sections in (a) and (b), respectively. The experimental lateral profile was obtained from the average of 6 central rows while the axial profile was obtained from the average of 16 axial profiles through the maxima. Intensity profiles were obtained after background subtraction followed by normalization. Case 2: xy and xz views of the numerical (e) and experimental (f) 3D image; lateral (g, h) and axial (i) intensity profiles obtained from the center (marked by the red arrows) of the xy and xz sections in (e) and (f), respectively. The cutoff frequency $u_c = 1.9 \mu\text{m}^{-1}$. Lateral and axial modulation frequencies: $u_m = 0.85 \mu\text{m}^{-1}$ and $w_m = 0.0135 \mu\text{m}^{-1}$ for Case 1; and $u_m = 1.33 \mu\text{m}^{-1}$ and $w_m = 0.021 \mu\text{m}^{-1}$ for Case 2.

2.3 Experimental validation of 3D image formation

Because the proposed excitation illumination pattern [Eq. (1)] is separable into axial and lateral functions, the intensity of a 3D image recorded by the camera in Fig. 1, $g(\mathbf{x}, z)$, can be expressed as [26]:

$$g(\mathbf{x}, z) = o(\mathbf{x}, z) \otimes_3 |h(\mathbf{x}, z)|^2 + \left\{ \cos(2\pi u_m(\eta)x + \phi) \times o(\mathbf{x}, z) \right\} \otimes_3 \left\{ |h(\mathbf{x}, z)|^2 \times \mathcal{V}(z; \eta, x_0, N) \right\}, \quad (3)$$

where $\mathbf{x} = (x, y)$ and z are the transverse and axial coordinates in the image volume, $o(\mathbf{x}, z)$ is the 3D density distribution of fluorophores within the sample volume, $|h(\mathbf{x}, z)|^2$ is the 3D PSF of the conventional widefield system, \otimes_3 stands for the 3D convolution operator, ϕ is the initial phase of the SI pattern, and

$$\mathcal{V}(z; \eta, x_0, N) = \frac{\sin(2\pi N w_m(\eta; x_0)z)}{N \sin(2\pi w_m(\eta; x_0)z)}, \quad (4)$$

where $w_m(\eta, x_0) = w'_m(\eta, x_0) / M_{ill}^2$ is the axial modulation frequency in the object space and it is proportional to the lateral modulation frequency, i.e. $w_m(\eta, x_0) = [u_m(\eta)x_0] / [2f_{L1}M_{ill}]$.

Without loss of generality, in Eq. (3) we assume that the lateral magnification of the detection imaging system (M) equal to 1. From Eq. (3) one realizes that the lateral illumination function modulates the object directly while the axial illumination function changes the axial behavior of the conventional PSF.

To validate the imaging performance of the experimental system we imaged two different test samples and compared the experimental 3D-SIM images with numerical results provided by Eq. (3). The first object is an axially-thin fluorescent layer, originally placed at an arbitrary distance z_0 in the object space, i.e., $o(\mathbf{x}, z) = \delta(z - z_0)$. For this case, the lateral and axial modulation frequency was $u_m = 0.44u_c = 0.85 \mu\text{m}^{-1}$ and $w_m = 0.0135 \mu\text{m}^{-1}$, respectively. The experimental axially-thin fluorescent layer was created by inserting a drop of a regular liquid fluorescent marker between a coverslip and a glass slide. The 3D numerical and experimental forward images are shown in Figs. 4(a) and (b), respectively. For a quantitative comparison, we measured the FWHM of the axial extent of the region where resonant planes are located [Figs. 4(a) and (b), xz -view images]. The axial extent for both cases is $2.3 \mu\text{m}$. Comparison of normalized intensity profiles along the lateral and axial directions show that experimental data is successfully predicted by the model [Figs. 4(c)-4(d)]. Note that the minimum background values were first subtracted.

For the second evaluation study, the test sample consisted of $6\text{-}\mu\text{m}$ in diameter spherical shells with a shell thickness equal to $1 \mu\text{m}$ (FocalCheck, Invitrogen, Molecular Probes, Carlsbad, CA) embedded in ProLong Diamond antifade mountant (Invitrogen, Molecular Probes) with a refractive index of 1.47. A detailed description of the sample preparation can be found in [13]. To better mimic the experimental conditions, we included spherical aberration ($w_{40} = 0.19$ which is computed as in [27]) in the simulated PSF. In addition, Poisson noise was incorporated in the forward image [28] resulting in a noisy image with a signal-to-noise ratio (SNR) of 18.5 dB, which is equal to the experimental SNR in Case 2 of Fig. 4. The average photons in the experimental data were estimated from the conversion datasheet provided by the camera's manufacturer and the SNR was computed by calculating the square root of the average photons over the entire 3D volume. Poisson noise was generated using the *poissrnd* built-in function of Matlab at a level comparable to the experimental data. For both simulated and experimental data we used a high lateral and axial modulation frequency $u_m = 0.7u_c = 1.33 \mu\text{m}^{-1}$ and $w_m = 0.021 \mu\text{m}^{-1}$ for $\eta = 50 \text{ mm}$. Note that both lateral and axial modulation frequencies have been increased by a factor of 1.6 over Case 1. Figures 4(e) and 4(f) show the corresponding xy and xz sections of the numerical and experimental data. Qualitative and quantitative agreement between the experimental and simulated 3D images is high, with only some evident discrepancies in the axial profiles depicted in panel (i). Thus, we conclude that the simulated data captures the trends in the experimental data.

2.4 Data processing

To provide a better understanding of our system's performance, we analyze the imaging process of our SIM implementation by taking the Fourier transform of Eq. (3) to obtain:

$$G(\mathbf{u}, w) = D_0(\mathbf{u}, w) + \frac{e^{i\phi}}{2} D_{+1}(\mathbf{u}, w) + \frac{e^{-i\phi}}{2} D_{-1}(\mathbf{u}, w), \quad (5)$$

where $\mathbf{u} = (u, v)$ and w are the transverse and axial frequency coordinates,

$$D_n(\mathbf{u}, w) = O(u - nu_m, v, w) H_n(\mathbf{u}, w), \quad n = 0, \pm 1, \quad (6)$$

and

$$H_n(\mathbf{u}, w) = \begin{cases} H(\mathbf{u}, w) & n = 0 \\ \text{FT}\left\{\left|h(\mathbf{x}, z)\right|^2 \mathcal{V}(z; \eta, x_0, N)\right\} & n = \pm 1 \end{cases} \quad (7)$$

FT{•} indicates the Fourier transform operation.

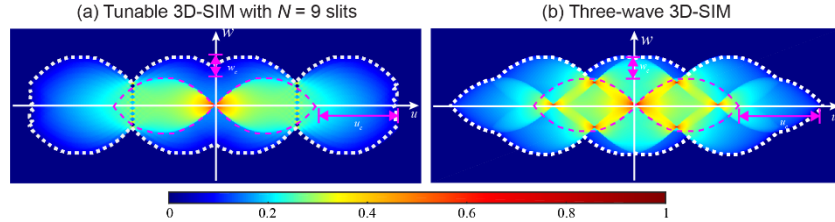


Fig. 5. Meridional section (uw) of the 3D synthetic MTF (absolute value of the synthetic OTF) for: (a) our 3D-SIM system with $N = 9$ slits; and (b) the conventional three-wave 3D-SIM system [1]. In both systems, we have considered the maximum lateral SR capability ($u_m = 0.8u_c$). Our synthetic OTF is composed of the 3 terms in Eq. (7). The pink and white dashed lines mark the compact support of the widefield and the 3D-SIM synthetic OTFs, respectively. The pink arrows highlight the extension of the lateral and axial cut-off frequencies achieved in both 3D-SIM synthetic OTFs.

Equation (7) shows the three terms that compose the effective synthetic OTF of our 3D-SIM system. The compact support of this synthetic OTF (Fig. 5(a), white dashed line) is comparable with the one achieved in three-wave interference (standard) 3D SIM (Fig. 5(b) white dashed line). Figure 5 shows that both the lateral and axial effective cut-off frequencies of our implemented system for $N = 9$ slits are equal with those of the standard 3D-SIM system. Additionally, this achieved OTF enlargement provides OS capability because the missing cone of frequencies present in the conventional OTF (Fig. 5, pink dashed line) is filled when 3D-SI is used. However, it is important to mention that the strength of the OTF for the three-wave 3D-SIM system [Fig. 5(b)] is greater, particularly in the axial direction, than the one observed in the OTF of the tunable 3D-SIM system with $N = 9$ slits [Fig. 5(a)]. Note that, without considering the widefield component, there are 6 replicas in the three-wave 3D-SIM OTF and 18 ($2N$) in our synthetic OTF. Based on the conservation of energy, it is clear that the strength of each OTF replica in our system would be lower than in each replica in the three-wave SIM OTF. In addition, as the location of the replica overlap varies, the overall strength in different regions of the two systems' OTFs is different. Nonetheless, in our system design one can engineer the compact support of the 3D OTF and its strength by designing the slit element. A more detailed analysis of how the slit element affects the compact support of our system's OTF will be reported in a future study.

Since the forward image's spectrum in tunable 3D SIM is composed by the sum of three shifted versions of the true sample's spectrum [Eq. (5)], only three forward images in which the SI pattern has been laterally shifted [ϕ in Eq. (3)] are needed to solve for the three unknown components, $D_n(\mathbf{u}, w)$. It is important to note that in the standard 3D SIM five images are needed to solve for five unique components. The standard reconstruction method for SIM [1] is based on a sequence of decomposition, deconvolution, shifting and recombination of these components. In our current system implementation, these unknown components are separated by solving a set of three linear equations and deconvolved using a generalized Wiener filter [1]:

$$\hat{D}_n(\mathbf{u}, w) = \frac{D_n(\mathbf{u}, w)H_n^*(\mathbf{u}, w)}{\sum_{n'} |H_{n'}(\mathbf{u} + n'u_m - n'u_m, v, w)|^2 + \beta^2} A(\mathbf{u} - n'u_m, v, w), \quad n = 0, \pm 1 \quad (8)$$

where $A(\mathbf{u}, w)$ is an apodization function that decreases linearly from unity at origin to zero at the border of the extended OTF support [1], $*$ denotes the conjugate operator, and β is a regularization parameter that needs to be adjusted empirically. Finally, the deconvolved components are shifted and combined properly (i.e., by ensuring that the energy of all deconvolved components is the same, thereby avoiding zeroth-order component dominance) to obtain the final restored image. To avoid undesired artefacts in the 3D restored image, the precise knowledge of the lateral modulation frequency and phase shifts in the modulated raw SIM images is critical. In experimental studies, we estimate these values by taking the Fourier transform of each raw SIM image and determining the phase associated with its sideband peaks [29].

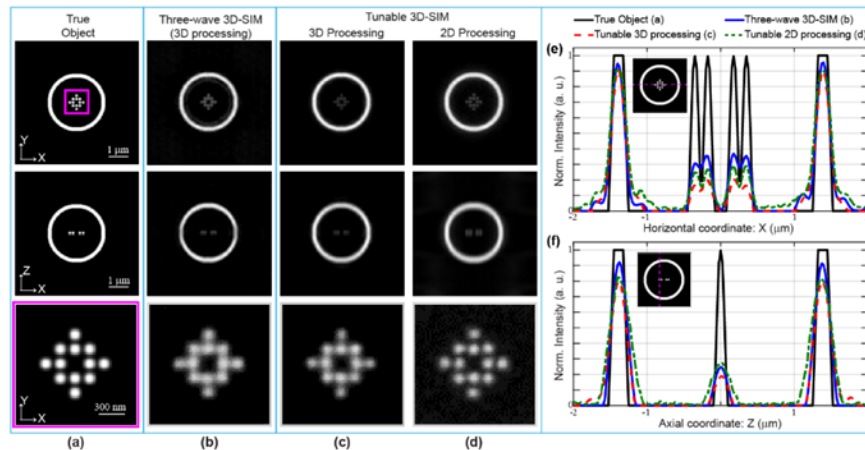


Fig. 6. Qualitative and quantitative evaluation of the proposed 3D-SIM system performance using simulated data. Lateral view (top row), axial view (middle row) and zoomed view of the cropped square marked with a pink line in the top left image (bottom row) of the 3D: (a) true object; (b) reconstructed image from three-wave interference 3D SIM; (c) reconstructed image from our 3D-SIM system; (d) reconstructed 3D image with proposed 2D processing method. Lateral (e) and axial (f) views of normalized intensity profiles. For both 3D-SIM systems, the lateral modulation frequency was set at $u_m = 0.8u_c = 4.35 \mu\text{m}^{-1}$.

Figure 6 evaluates the performance of our 3D-SIM system and compares it to the performance of the standard 3D-SIM system [1] through restoration from simulated images of a numerical 3D test object. The 3D object was computed to mimic a cell's structure in biological studies. It is composed by an outer spherical shell (diameter = 3 μm and thickness = 200 nm) and inner spherical beads whose diameter is 125 nm. To show SR performance, the distance between two neighboring beads is equal to 100 nm, which is below the resolution limit of the conventional widefield microscope ($\lambda/2\text{NA} = 184 \mu\text{m}$ for an emission wavelength of $\lambda = 515 \text{ nm}$ and an imaging lens' NA = 1.4). In this numerical study, the phase ϕ of the SI pattern is changed by $2\pi/3$ for the 3 phase images in the tunable 3D-SIM system and $2\pi/5$ for the 5 phase images needed in three-wave 3D SIM along three orientation angles of the pattern ($\theta = 0^\circ, 60^\circ$ and 120°) to achieve isotropic resolution improvement. Furthermore, Poisson noise was introduced in the forward image [28] resulting in a SNR of 18.5 dB (equal to the experimental SNR in Case 2 of Fig. 4). The regularization parameter was empirically determined and it was set equal to $\beta = 0.002$. Negative values in the restored images due to Wiener filtering were set to zero. Qualitative observation of the 3D restored images from both systems [Figs. 6(b)-6(c)] as well as comparison of intensity profiles through them [Figs. 6(e)-6(f)] indicate that the overall performance of both systems is quite comparable. These results are consistent with the comparison of the two systems' synthetic-OTF compact support (Fig. 5).

The restoration method mentioned above [Eq. (8)] is used when the entire 3D image of the object is captured. However, if only some raw 2D images are available, one can approximately restore the object information by 2D processing at each plane using either the 2D generalized Wiener filter [26] or the approach in [30]. The latter works well if only the in-focus information is modulated with the SI pattern, i.e., when the SI pattern is axially confined. This approach is valid if the axial extent of the SI pattern is smaller than or comparable to the depth of field of the imaging lens used. In our current implementation, both values are equal; the theoretical depth of field (λ/NA^2) for the $20\times/0.5$ NA objective lens is $2.06\ \mu\text{m}$ and the axial extent of the pattern for 9 slits is $2.1\ \mu\text{m}$ (Fig. 3). Therefore, using a similar approach as the one in [30] we compute a new data set of forward images in which the out-of-focus information has been removed. Using these pre-processed raw SIM images, we obtain the final restored image by applying the same process of demodulation, shifting and combining of the retrieved frequency components as before [26] but without the final deconvolution. The pre-processing is based on the method in [30] but our approach in computing components that are mathematically equivalent to the ones reported in Eqs. (4) and (5) of [30] is different. In our approach, we first deconvolve each 2D raw image by applying a 2D Wiener filter with the non-aberrated 2D PSF at the best focal plane to remove the diffraction effects of the PSF [31]. Note that each deconvolved raw image $g'(x)$ is still expressed by the sum of three unknown components, $\{d_n'(x, z)\}$, which are then decomposed by solving a set of linear equations to provide the unmodulated part, $d_0'(x, z)$, and the in-focus optically-sectioned demodulated content, $e^{-i2\pi u_m x} d_{+1}'(x, z) + e^{i2\pi u_m x} d_{-1}'(x, z)$.

Figure 6(d) shows the 3D restored image of the numerical test object obtained by stacking all the transverse planes after applying the 2D processing method. The regularized parameter in the 2D Wiener filtering of step 1 of the method was empirically determined to be equal to 0.05. Interestingly, the zoomed view of the cropped square in the xy -section image from this 3D restored image (Fig. 6(d), bottom row) shows qualitative improvement over the result obtained with the 3D processing method (Fig. 6(c) bottom row). However, as expected the 3D method provides better axial performance than the 2D processing method. A comparison of the intensity profiles through the center of the restored images discussed in this section [Fig. 6(e) and 6(f)] confirms qualitative observations.

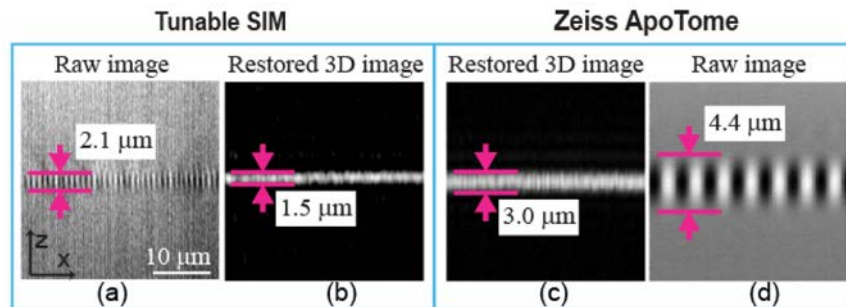


Fig. 7. Achieved OS capability verified with experimental images of an axially-thin fluorescent layer: xz -sections of the raw (a and d) and restored SIM image (b and c) from the tunable 3D-SIM ($u_m = 0.8u_c$) and the ApoTome-SIM ($u_m = 0.14u_c$) systems. Because ApoTome processing does not consider the widefield component, which is equivalent to the $\hat{D}_0(\bullet)$ component [Eq. (8)], we neglected this term when computing the restored image in the case of our system (b) for a fair comparison. In panels (a) and (d), the pink arrows indicate the axial extent of the SI pattern, quantified by the value shown on each image. The pink arrows in panels (b) and (c) quantify the FWHM of the integrated intensity, obtained by averaging the intensity values along its lateral coordinate for each restored image.

3. Proof-of-concept experimental results

In this section, we present reconstructed images obtained from three proof-of-concept experimental data sets recorded using a $20\times/0.5$ NA dry objective lens. The 3D SI pattern was generated using 9 slits and the position of the Fresnel biprism was set at $\eta = 56$ mm to achieve the highest lateral and axial modulation frequencies, $u_m = 0.8u_c = 1.55 \mu\text{m}^{-1}$ and $w_m = 0.049 \mu\text{m}^{-1}$, respectively. Results from the proposed 3D-SIM system are also compared to results obtained from the same test samples with a commercial commercial incoherent grid-projection system [24] (ApoTome.2 SIM module on a Zeiss AxioImager.Z2 upright available in our laboratory) to validate its performance. To acquire the 3D data set of the sample under research with the commercial ApoTome-SIM system, we used the L-illumination grating, which provides the highest available lateral modulation frequency ($u_m = 0.14u_c = 0.27 \mu\text{m}^{-1}$), and an axial scanning interval equal to $0.3 \mu\text{m}$. The final 3D image from the commercial system was restored using the ApoTome deconvolution method (Zeiss ZEN.2 software [32]).

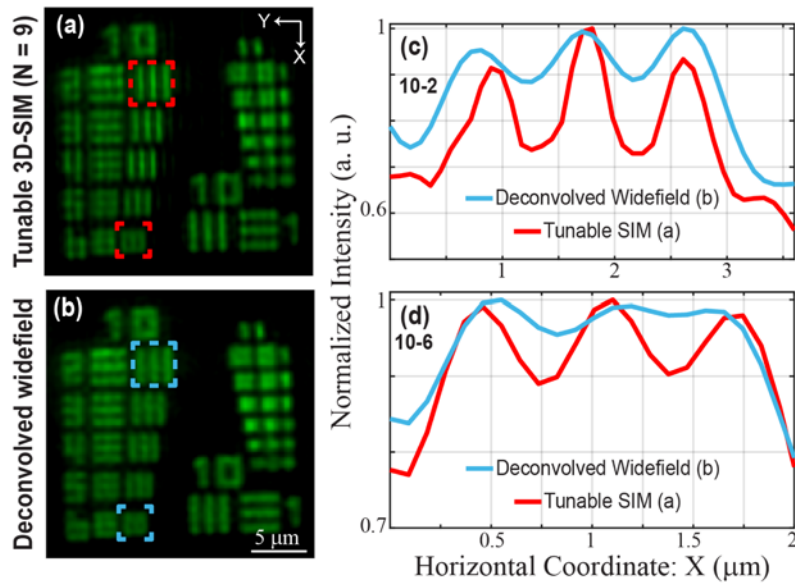


Fig. 8. Achieved SR verified in experimental images of the fluorescent USAF target: (a) Reconstructed SIM image for $u_m = 0.8u_c$ and (b) Synthetic deconvolved widefield image. (c) and (d) Normalized intensity profiles through the center of the vertical elements 10-2 and 10-6, marked by the dashed rectangles in (a) and (b), from both images.

The first experiment evaluates the OS capability of our system. The OS capability was evaluated using the integrated intensity [33], which relates the total power in out-of-focus planes with the power in the in-focus plane. Experimentally, the integrated intensity is measured by axially scanning an axially-thin fluorescent layer in the object space. Figure 7 shows xz -section images from an axially-thin fluorescent layer. As evident from these images our SIM implementation [Fig. 7(a)] can operate like the ApoTome system [Fig. 7(d)] because it has a confined SI pattern but with a 40% reduced axial extent due to the larger modulation frequency that can be used in our system compared to the ApoTome system. Since fewer transverse sections of the sample are modulated by the SI pattern, our 3D-SIM system can provide better discrimination of the out-of-focus light than ApoTome SIM. The corresponding reconstructed images of the fluorescent layer in Figs. 7(b) and (c) allow quantitative comparison of the OS capability of the two systems using the integrated intensity (computed by averaging the intensity values along the lateral coordinate for each axial position of the layer). The measured FWHM of the integrated intensity is $1.5 \mu\text{m}$ and $3 \mu\text{m}$

for the proposed 3D-SIM and ApoTome-SIM systems, respectively. Because the narrower the integrated intensity, the higher the OS capability, one can conclude that our system determines more accurately the layer's axial position than the commercial ApoTome-SIM system.

The achieved SR capability of our system is validated experimentally with SIM images acquired from an extreme USAF target (Ready Optics, Calabasas, California) whose metallic surface was painted with fluorescent dye. Figure 8 shows the reconstructed SIM image [Fig. 8(a)] and the deconvolved synthetic widefield image (obtained from the zero-order component) [Fig. 8(b)]. The smallest resolved element of group 10 in Figs. 8(a) and 8(b) provides the lateral resolution limit achieved in each case. The resolution has been increased from 1149 lp/mm (element 2 of group 10) in the deconvolved synthetic widefield image) to 1825 lp/mm (element 6 of group 10) in the image from our 3D-SIM system. Note that the corresponding resolvable distance of these elements is 435 nm and 274 nm, respectively. Normalized intensity profiles along the horizontal direction through the center of these vertical elements of group 10 [10-2 and 10-6 marked by the dashed rectangles in Figs. 8(a)-8(b)] from both images are plotted in panels (c) and (d), respectively, to confirm the resolution limit in each case. As it is expected, the use of the SIM technique almost doubles the resolution limit of the native system when the lateral modulation frequency of the SI pattern is close to the cutoff frequency of the imaging system ($u_m = 0.8u_c$). Particularly, the smallest resolvable distance has been reduced by a factor of 1.8 (from 515 nm, which is the diffraction limit for an emission wavelength of $\lambda = 515$ nm and an imaging lens' NA = 0.5, to 274 nm) for the native system and 1.6 (from 435 nm to 274 nm) after applying deconvolution. Note that the lateral SR performance of our proposed 3D-SIM system is comparable with the performance of a standard 3D-SIM system. From the spectrum shown in Fig. 3(a) of [34], one can estimate that the lateral resolution of a commercial Zeiss Elyra PS.1 system has been improved by a factor of 1.7, which would correspond to a lateral modulation frequency of $u_m = 0.7u_c$ independent of the objective lens used.

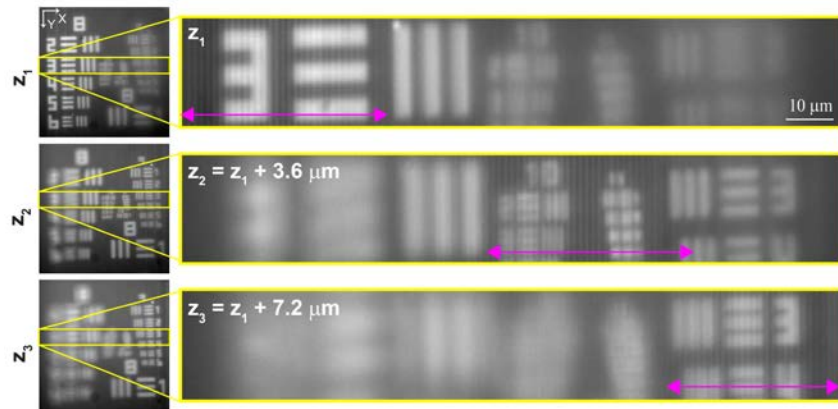


Fig. 9. Experimental raw images of a tilted fluorescent USAF target at three different axial positions (z_i). Note that the fringes are visible only in the region of the FoV where the target is in-focus, marked by the pink double arrow in the zoomed versions of the areas marked by the yellow rectangles in the images shown on the left.

Finally, in our last experiment, simultaneous OS and SR capabilities are verified using a tilted fluorescent USAF target. The induced tilt is ~ 6.5 degrees with respect to the optical axis to create an object with axial variability. Figure 9 shows experimental raw SIM images obtained at three different axial positions of the target using our 3D-SIM system. As expected, the SI pattern is visible only where the tilted USAF target is in-focus in each transverse plane image.

The experimental 2D raw images for these three axial positions (Fig. 9) in our system have been reconstructed using the 2D processing method described in Sect. 2.4 (see results in Fig. 10). To quantify the achieved OS we determine the reduction in the out-of-focus information by computing and comparing the integrated intensity inside the different magenta rectangles illustrated in Figs. 10(a)-10(b). Note that different elements are marked by the rectangles in each focal plane to assess regions where we do not expect in-focus information such as: the vertical elements of group 8 in the first column, the numbers and horizontal elements of group 8 in the second column, and the groups 10 and 11 in the last column. Figure 10(a) shows the synthetic raw widefield image (e.g., the estimated widefield image from the raw SIM data without applying any deconvolution method), which contains out-of-focus information since the imaging system does not have any OS capability. Nonetheless, in the reconstructed image from tunable 3D-SIM system [Fig. 10(b)] the out-of-focus information has been reduced by at least 70%.

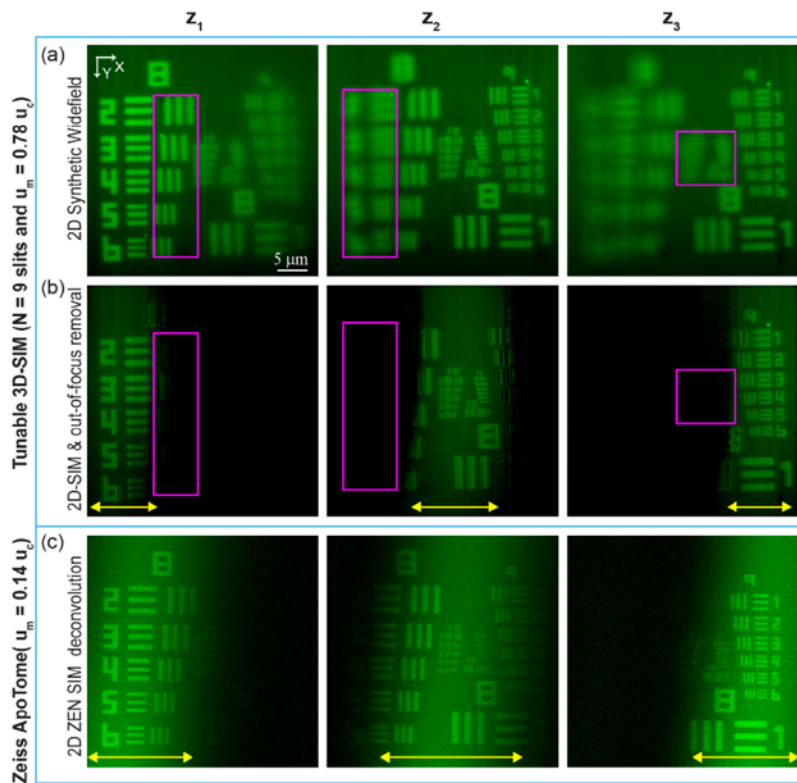


Fig. 10. Experimental verification of simultaneous OS and SR achieved with our tunable 3D-SIM system by imaging a tilted fluorescent USAF target. xy -sections images obtained at three different axial locations of the target: (a) Synthetic raw widefield images; (b) Reconstructed SIM images from our systems using 2D processing (Sect. 2.4); (c) Reconstructed ApoTome-SIM images using the Zeiss ZEN.2 software. The corresponding magenta rectangles in (a) and (b) highlight the reduction of out-of-focus light achieved in the tunable 3D-SIM system image (b) compared to the conventional widefield image (a). The rectangles highlight different regions of the FoV in which in-focus information is not expected in each axial location of the tilted target. The yellow arrows indicate the lateral extent of the FoV reconstructed in the final image. The images in each case (a), (b) and (c) are displayed using a separate color scale. However, the group of three images in (a), (b), and (c), respectively, are displayed using a global minimum and maximum relative intensity mapped to the same color scale to show relative intensities in different axial planes. Lens: $20\times/0.5$ NA dry lens; Emission wavelength: 515 nm. Lateral modulation frequency: $u_m = 0.8u_c = 1.552 \mu\text{m}^{-1}$ for the tunable 3D-SIM system and $u_m = 0.14u_c = 0.27 \mu\text{m}^{-1}$ for the commercial ApoTome-SIM system.

To finalize this study, we compared the restored images from this tilted object obtained with our proposed SIM system [Fig. 10(b)] and the Zeiss ApoTome system [Fig. 10(c)]. The portion of the retrieved information for each transverse section, marked by the yellow arrows in panels (b) and (c) of Fig. 10, is narrower in the images from our system than in the ones from the ApoTome-SIM system. In fact, the reconstructed FoV in the images shown in Fig. 10(c) is larger than those in Fig. 10(b) by a factor of $1.56 \times$, $1.63 \times$ and $1.65 \times$ for the three different transverse positions (z_i). This restored FoV is proportionally related to the axial extent of the SI pattern (Fig. 9). As expected, the narrower the axial extent of the SI pattern, the narrower the reconstructed FoV in each transverse section and, consequently, the higher the ability of the system to determine the axial position of each lateral feature. Following this reasoning, one could claim that our system provides better OS capability. Note that this conclusion agrees with the result in Fig. 7. Figure 11 shows the resolution achieved in the tilted USAF target images from our 3D-SIM system. The measured lateral resolution limit ranges between 308 nm and 345 nm, which exceeds the diffraction limit by a factor of $1.5 \times$. Thus, simultaneous OS and SR capabilities of our 3D-SIM system are verified with this experiment.

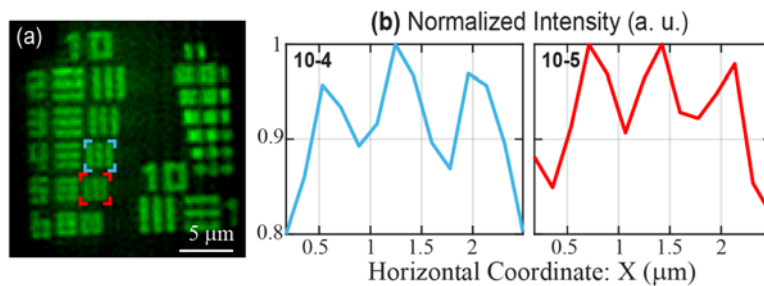


Fig. 11. Verification of the lateral SR capability in the experimental image of the tilted fluorescent USAF target: (a) zoomed version of the groups 10 and 11 in the reconstructed SIM image obtained at the axial location z_2 in Fig. 10(b). (b) Normalized intensity profiles through the center of the vertical elements 10-4 and 10-5, marked by light blue and red dashed rectangles, along the horizontal direction.

4. Conclusions

In this work an incoherent-based 3D-SIM system that provides high-contrast structured illumination patterns localized at discrete axial planes was presented and its performance was investigated numerically and experimentally. The 3D SI pattern in this system is generated by illuminating a Fresnel biprism using the emerging light coming from multiple spatially-incoherent slits. An advantage of the system is that both lateral and axial periodicities of the 3D fringes can be tuned independently, providing axial SR capability independent of the lateral SR performance. While both lateral and axial periodicities of the pattern can be continuously tuned by axially displacing the biprism, the axial periodicity of the pattern can be independently tuned by the choice of the slits' separation (x_0). A more detailed study of this axial tunability will be reported in a future publication. Here, we provide proof-of-concept studies using a low-NA implementation and for the particular design of $N = 9$ slits and $x_0 = 100 \mu\text{m}$. In the investigated studies, we showed that the narrower the axial extent of the fringes, the better discrimination of out-of-focus light is achieved (improved OS capability) in the final restored image of an axially-thin fluorescent layer. Additionally, the proposed tunable 3D-SIM system is shown to provide an increase in the lateral resolution limit by a factor of $1.8 \times$ compared to the native system, which is comparable with the performance of a commercial 3D-SIM system [34], and improved OS capability by a factor of $1.6 \times$ compared to the ApoTome-SIM system. Nonetheless, the main hallmark of the proposed 3D-SIM system is that it requires fewer images for the final restoration than the three-wave interference 3D-SIM system, which is the golden standard, while the performance

of both systems appears to be comparable based on the compact support of the synthetic OTF comparison and numerical results from reconstruction of simulated data. Note that our final SIM image is restored using 40% less data since only three phase-shifted images are needed per orientation of the pattern, as opposed to the five images required by the standard 3D-SIM system. Although we have not rotated the 3D SI pattern to achieve isotropic resolution improvement, the pattern can be rotated by jointly rotating the slits' element and the Fresnel biprism or, in a more practical way, by inserting a Dove prism [35] in the SI system and rotating it. To avoid the mechanical movement of the Dove prism, one could use an acousto-optic Dove prism [36]. Because the approaches to provide the needed phase shifting and the rotation of the SI pattern are already available, and implemented in commercial 3D-SIM systems, we believe that a commercial prototype of our tunable 3D-SIM system (e.g. with similar components as those used in commercial 3D-SIM systems) should operate 40% faster than commercially-available systems due to the 40% reduction in the data required for restoration. Additionally, by taking advantage of symmetries and redundancies, we expect that a reduction in the number of images, required for isotropic resolution, from 9 to 4 could also be possible, and future studies will investigate this additional data reduction to make our tunable 3D-SIM system better suited for live-cell imaging.

Funding

National Science Foundation (NSF) (DBI award 1353904, PI: CP); the University of Memphis; Ministerio de Economía y Competitividad, Spain (DPI2015-66458-C2-1-R); Generalitat Valencia (PROMETEOII/2014/072).

Acknowledgments

We thank collaborators S. V. King (St. Jude Children's Research Hospital, Memphis, TN) and M. Martínez-Corral (Univ. of Valencia, Spain) for scientific and technical discussion.

References

1. M. G. L. Gustafsson, L. Shao, P. M. Carlton, C. J. R. Wang, I. N. Golubovskaya, W. Z. Cande, D. A. Agard, and J. W. Sedat, "Three-dimensional resolution doubling in wide-field fluorescence microscopy by structured illumination," *Biophys. J.* **94**(12), 4957–4970 (2008).
2. C. J. R. Wang, P. M. Carlton, I. N. Golubovskaya, and W. Z. Cande, "Interlock formation and coiling of meiotic chromosome axes during synapsis," *Genetics* **183**(3), 905–915 (2009).
3. K. F. Sonnen, L. Schermelleh, H. Leonhardt, and E. A. Nigg, "3D-structured illumination microscopy provides novel insight into architecture of human centrosomes," *Biol. Open* **1**(10), 965–976 (2012).
4. V. O. Chagin, C. S. Casas-Delucchi, M. Reinhart, L. Schermelleh, Y. Markaki, A. Maiser, J. J. Bolius, A. Bensimon, M. Fillies, P. Domaing, Y. M. Rozanov, H. Leonhardt, and M. C. Cardoso, "4D Visualization of replication foci in mammalian cells corresponding to individual replicons," *Nat. Commun.* **7**, 11231 (2016).
5. A. C. N. Brown, S. Oddos, I. M. Dobbie, J. M. Alakoskela, R. M. Parton, P. Eissmann, M. A. A. Neil, C. Dunsby, P. M. W. French, I. Davis, and D. M. Davis, "Remodelling of cortical actin where lytic granules dock at Natural Killer cell immune synapses revealed by super-resolution microscopy," *PLoS Biol.* **9**(9), e1001152 (2011).
6. V. C. Cogger, G. P. McNerney, T. Nyunt, L. D. DeLeve, P. McCourt, B. Smedsrød, D. G. Le Couteur, and T. R. Huser, "Three-dimensional structured illumination microscopy of liver sinusoidal endothelial cell fenestrations," *J. Struct. Biol.* **171**(3), 382–388 (2010).
7. V. W. Rowlett and W. Margolin, "3D-SIM super-resolution of FtsZ and its membrane tethers in *Escherichia coli* cells," *Biophys. J.* **107**(8), L17–L20 (2014).
8. C. Lesterlin, G. Ball, L. Schermelleh, and D. J. Sherratt, "RecA bundles mediate homology pairing between distant sisters during DNA break repair," *Nature* **506**(7487), 249–253 (2014).
9. J. Tilsner, O. Linnik, M. Louveaux, I. M. Roberts, S. N. Chapman, and K. J. Oparka, "Replication and trafficking of a plant virus are coupled at the entrances of plasmodesmata," *J. Cell Biol.* **201**(7), 981–995 (2013).
10. L. M. Hirvonen, K. Wicker, O. Mandula, and R. Heintzmann, "Structured illumination microscopy of a living cell," *Eur. Biophys. J.* **38**(6), 807–812 (2009).
11. P. Kner, B. B. Chhun, E. R. Griffis, L. Winoto, and M. G. L. Gustafsson, "Super-resolution video microscopy of live cells by structured illumination," *Nat. Methods* **6**(5), 339–342 (2009).
12. R. Fiolka, L. Shao, E. H. Rego, M. W. Davidson, and M. G. L. Gustafsson, "Time-lapse two-color 3D imaging of live cells with doubled resolution using structured illumination," *Proc. Natl. Acad. Sci. U.S.A.* **109**(14), 5311–5315 (2012).

13. H. Shabani, A. Doblas, G. Saavedra, E. Sanchez-Ortiga, and C. Preza, "Improvement of two-dimensional structured illumination microscopy with an incoherent illumination pattern of tunable frequency," *Appl. Opt.* **57**(7), B92–B101 (2018).
14. R. Heintzmann, "Saturated patterned excitation microscopy with two-dimensional excitation patterns," *Micron* **34**(6-7), 283–291 (2003).
15. F. Orieux, E. Sepulveda, V. Lorient, B. Dubertret, and J. C. Olivo-Marin, "Bayesian estimation for optimized structured illumination microscopy," *IEEE Trans. Image Process.* **21**(2), 601–614 (2012).
16. S. Dong, J. Liao, K. Guo, L. Bian, J. Suo, and G. Zheng, "Resolution doubling with a reduced number of image acquisitions," *Biomed. Opt. Express* **6**(8), 2946–2952 (2015).
17. J. Boulanger, N. Pustelnik, L. Condat, L. Sengmanivong, and T. Piolot, "Nonsmooth convex optimization for structured illumination microscopy image reconstruction," *Inverse Probl.* **34**(9), 095004 (2018).
18. A. Lal, C. Shan, K. Zhao, W. Liu, X. Huang, W. Zong, L. Chen, and P. Xi, "A Frequency Domain SIM Reconstruction Algorithm Using Reduced Number of Images," *IEEE Trans. Image Process.* **27**(9), 4555–4570 (2018).
19. F. Orieux, V. Lorient, J. C. Olivo-Marin, E. Sepulveda, and A. Fragola, "Fast myopic 2D-SIM super resolution microscopy with joint modulation pattern estimation," *Inverse Probl.* **33**(12), 1–22 (2017).
20. A. Doblas, G. Saavedra, M. Martínez-Corral, J. C. Barreiro, E. Sanchez-Ortiga, and A. Llavador, "Axial resonance of periodic patterns by using a Fresnel biprism," *J. Opt. Soc. Am. A* **30**(1), 140–148 (2013).
21. H. Shabani, A. Doblas, G. Saavedra, and C. Preza, "Preprocessing method to correct illumination pattern in sinusoidal-based structured illumination microscopy," *Proc. SPIE* **10499**, 104991Z (2018).
22. A. Doblas and C. Preza, "Incoherent-based tunable frequency structured illumination microscopy," in *IS Conference of 2017 OSA Technical Digest Series (Optical Society of America)* (2017), paper ITh4.
23. H. Shabani, A. Doblas, G. Saavedra, and C. Preza, "3D structured illumination microscopy using an incoherent illumination system based on a Fresnel biprism," *Proc. SPIE* **10499**, 1049903 (2018).
24. M. A. A. Neil, R. Juskaitis, and T. Wilson, "Method of obtaining optical sectioning by using structured light in a conventional microscope," *Opt. Lett.* **22**(24), 1905–1907 (1997).
25. J. W. Goodman, *Introduction to Fourier Optics* (McGraw-Hill, 1996).
26. H. Shabani, N. Patwary, A. Doblas, G. Saavedra, and C. Preza, "Comparison of two structured illumination techniques based on different 3D illumination patterns," *Proc. SPIE* **10070**, 1007013 (2017).
27. G. Saavedra, I. Escobar, R. Martínez-Cuenca, E. Sánchez-Ortiga, and M. Martínez-Corral, "Reduction of spherical-aberration impact in microscopy by wavefront coding," *Opt. Express* **17**(16), 13810–13818 (2009).
28. M. Bertero, P. Boccacci, G. Desidera, and G. Vicidomini, "Image deblurring with Poisson data: from cells to galaxies," *Inverse Probl.* **25**(12), 123006 (2009).
29. S. A. Shroff, J. R. Fienup, and D. R. Williams, "Phase-shift estimation in sinusoidally illuminated images for lateral superresolution," *J. Opt. Soc. Am. A* **26**(2), 413–424 (2009).
30. P. Vermeulen, H. Zhan, F. Orieux, J. C. Olivo-Marin, Z. Lenkei, V. Lorient, and A. Fragola, "Out-of-focus background subtraction for fast structured illumination super-resolution microscopy of optically thick samples," *J. Microsc.* **259**(3), 257–268 (2015).
31. N. Patwary, A. Doblas, and C. Preza, "Image restoration approach to address reduced modulation contrast in structured illumination microscopy," *Biomed. Opt. Express* **9**(4), 1630–1647 (2018).
32. L. H. Schaefer and D. Schuster, "Method and device for reconstructing images," U.S. Patent No. 8,041,142 (2011).
33. M. Martínez-Corral and G. Saavedra, "The Resolution Challenge in 3D Optical Microscopy," *Prog. Opt.* **53**, 1–67 (2009).
34. C. Karras, M. Smedh, R. Förster, H. Deschout, J. Fernandez-Rodriguez, and R. Heintzmann, "Successful optimization of reconstruction parameters in structured illumination microscopy - a practical guide," *bioRxiv* **402115**, 1–13 (2018).
35. E. Hecht, *Optics* (Pearson, 2016).
36. E. G. Paek, J. Y. Choe, T. K. Oh, J. H. Hong, and T. Y. Chang, "Nonmechanical image rotation with an acousto-optic dove prism," *Opt. Lett.* **22**(15), 1195–1197 (1997).